

MIT Open Access Articles

Design of a Novel Multiple-DOF Extendable Arm With Rigid Components Inspired by a Deployable Origami Structure

The MIT Faculty has made this article openly available. **Please share** how this access benefits you. Your story matters.

Citation: Matsuo, Hiroshi et al. "Design of a Novel Multiple-DOF Extendable Arm With Rigid Components Inspired by a Deployable Origami Structure." IEEE Robotics and Automation Letters 5, 2 (April 2020): 2730 - 2737. © 2020 IEEE

As Published: <http://dx.doi.org/10.1109/lra.2020.2970976>

Publisher: Institute of Electrical and Electronics Engineers (IEEE)

Persistent URL: <https://hdl.handle.net/1721.1/127998>

Version: Author's final manuscript: final author's manuscript post peer review, without publisher's formatting or copy editing

Terms of use: Creative Commons Attribution-Noncommercial-Share Alike



Design of a Novel Multiple-DOF Extendable Arm with Rigid Components Inspired by a Deployable Origami Structure*

Hiroshi Matsuo¹, H. Harry Asada² and Yukio Takeda¹

Abstract—An extendable robot inspired by origami is designed, analyzed, and tested. Its deployable origami structure has a large extension ratio, allowing the robot to extend the body length multiple times. The new robot, however, differs from the existing origami structure in two aspects. One is that the robot mechanism consists of all rigid bodies, unlike the prior origami that exploits structural deformation for creating flexible configurations. The other is that new origami-inspired robot has multiple active degrees of freedom, allowing for taking various postures, unlike most deployable mechanisms composed of rigid components having a single DOF. When developing a mechanism based on an origami structure, we often encounter the deformations of parts during the transition from the contracted to the extended configurations. Previously, we analyzed the motion of a deployable origami structure considering the foldings' deformation and showed that they do not have any kinematic roles but give a large effect to constrain the motion. Thus, we come to the idea that by removing such parts, a novel rigid extendable mechanism with multiple DOF can be obtained, which can achieve a large extension ratio and a high transformability only by its kinematic structure, beyond an original origami structure.

Index Terms—Mechanism Design, Kinematics

I. INTRODUCTION

IN heavy industries, such as the automobile and aviation industries, a majority of the manufacturing processes are automated. However, a few heavy tasks, such as assembly, inspection, and maintenance, occur in narrow spaces where workers may be unable to view the workspace. Such tasks have been manually performed by workers and involve inconvenient postures that may lead to injuries. As a solution to this problem, a robot arm that can replace such manual labor is proposed, based on the concept of an extendable arm that can bear reaction forces and perform heavy tasks by exploiting the contact force with narrow spaces. This concept is depicted in Fig. 1. The primary requirements of extendable arms are high extendability and transformability. In addition, a sufficient load

capacity is required when performing such tasks. To develop this extendable arm, a practical mechanism that satisfies the requirements mentioned above is needed, and the usability of such a mechanism needs to be validated. In this paper, we introduce the design of a novel extendable mechanism in which characteristics of inspired origami structures has been expanded by solving problems associated with deployable origami structures.

Deployable origami structures have attracted attention as base structures of transformable applications due to their high extendability and high transformability. In general, deployable origami structures are roughly divided into two types: rigid-foldable origami and soft-deployable origami. The former is foldable without any deformations in its components, such as the famous Miura-ori [1]. Several methods have been developed to fold the structure as small as possible with thick panels [2]–[4]. Most rigid-foldable mechanisms only have a single degree of freedom (DOF) and mainly focus on two configurations; fully contracted and extended [5], [6]. The latter is deployable and transformable, such as the example

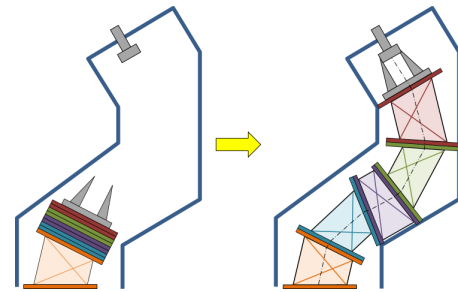


Fig. 1. Conceptual design of the extendable arm that can bear reaction forces and perform heavy labor by exploiting the contact forces with narrow spaces.

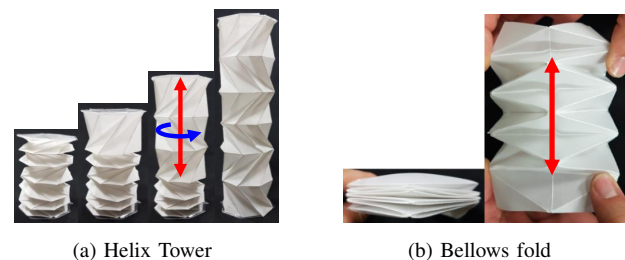


Fig. 2. Representative deployable cylindrical origami structures. This structure can be extended by pulling it along the longitudinal direction and/or rotating each segment.

Manuscript received: September, 10, 2019; Revised December, 20, 2019; Accepted January, 19, 2020.

This paper was recommended for publication by Editor Paolo Rocco upon evaluation of the Associate Editor and Reviewers' comments.

*A part of this work has been supported by the Grants-in-Aid for Scientific Research 18J21466 and NSK Ltd.

¹ Department of Mechanical Engineering, Tokyo Institute of Technology, 2-12-1 Ookayama, Meguro-ku, Tokyo, 152-5882, Japan {matsuo.h.ae, takeda.y.aa}@m.titech.ac.jp

² Department of Mechanical Engineering, Massachusetts Institute of Technology, Cambridge, MA 02139, USA asada@mit.edu

Digital Object Identifier (DOI): see top of this page.

shown in Fig. 2, and several types of extendable applications have been developed based on such origami structures to assist daily living activities with thin materials [7]–[10]. However, their deployment and shape transformation, which look like multiple DOF motion, are achieved thanks to its material flexibility, not only to its kinematic structure. In other words, deformations, especially buckling, occur in the foldings and facets [11], and the motion of the structure becomes discontinuous by buckling. This buckling occurs because the length of the sides does not change when transitioning from the contracted to the extended configurations. Previous studies on shock absorption [12] and vibration isolators [13] have exploited this phenomenon of buckling.

To develop the extendable arm such as shown in Fig. 1, both types of deployable origami structures are insufficient because they cannot simultaneously satisfy all the primary requirements: high extendability, high transformability with multiple DOF and sufficient load capacity. Here, we have come to an idea that by removing the constraints and constructing with rigid components, we could obtain a novel extendable mechanism which takes the advantage of both types of deployable origami structure and satisfies all the primary requirements.

Based on the concept above, this paper presents a design of a novel rigid extendable arm, which has a large extension ratio, multiple DOF, and a high transformability given by its kinematic structure, beyond those of an inspired deployable origami structure, the origami spring [14] (Fig. 3). Its effectiveness is investigated through displacement analysis and motion experiments, using an actuated prototype. Kinematic design of the proposed mechanism has been supported by some ideas to maximize its workspace and methods to calculate the actual DOF. We also discuss an idea for its actuation and its validity has been confirmed by the selection of active joints.

II. MECHANISM DESIGN AND MODELING

A. Features of the Origami Spring

The origami spring is an deployable origami structure, and the entire structure is extended by reducing its circumference, as shown in Fig. 3. Moreover, its folding diagram consists of unit right angled triangles, as shown in Fig. 4, where a is the length of the longitudinal side, b is the length of the lateral side, m is the number of segments, the example in Fig. 3 consists of four segments, and n is the number of sides of the regular polygon ($n \geq 6$) when the origami spring is fully contracted. $\varphi = \pi/n$ is the smallest angle of the unit right angled triangle. When the folded edges are regarded as revolute joints, the origami spring is kinematically modelled as a spherical closed-loop mechanism with three DOF [15].

In this kinematic model, the hypotenuse of the unit right angled triangle should be modelled as a compliant string because it always deforms due to collisions with other hypotenuses. We revealed that the actual motion of the origami spring, a macroscopic single DOF motion, is the result of constraint by the hypotenuse although it does not have any kinematic role. This fact can be theoretically explained by considering the deformation and potential energy of the hypotenuse string [16].

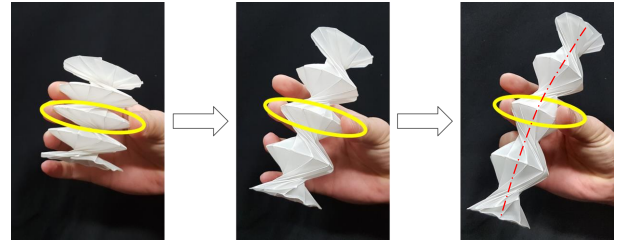


Fig. 3. Motion of an origami spring by reducing its circumference [16]

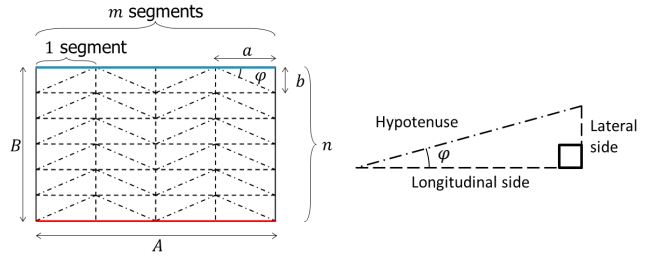


Fig. 4. Folding diagram and unit right angled triangle [15], [16]

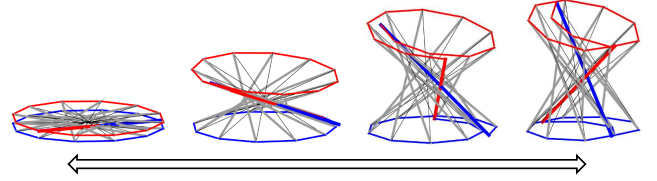


Fig. 5. Coiling and tilting motions during extension of the original mechanism. At the extension limit, the three lateral sides are coiled inside, and the nine ones remain outside about the lower and upper lateral chains.

Based on our previous study, by removing the hypotenuse, the origami spring becomes a suitable structure to be applied to an rigid extendable arm, which has a large extension ratio, multiple DOF, and a high transformability given by its kinematic structure. In addition, it is easier to actuate the origami spring as compared to other deployable cylindrical origami structures, on removing the part at which undesired deformations occur. On the contrary, there are a few disadvantages associated with using an origami spring. These disadvantages include the coiling and tilting motions during extension, as shown in Fig. 5. These two motions are dependent on each other and caused due to the collision of components, especially the longitudinal sides, thereby leading to a reduction of the workspace.

B. Improvement to maximize performance

To exploit the features of the origami spring and achieve maximum performance as an extendable arm, we addressed the three issues by modifying its design: deformation of the hypotenuse, coiling motion, and collision between components. The origami spring where $m = 1$ and $n = 12$ is referred as the base structure.

First, the hypotenuses of the unit right angled triangles were removed, as shown in Fig. 6. The deformation of the hypotenuse and the resulting stored potential energy causes

the configuration during extension and contraction to be symmetric to the plane between two segments. By removing the hypotenuses, the mechanism can possess complete three DOF and take all configurations in the workspace. Furthermore, the symmetry between segments also breaks.

Second, six unit triangles, which are coiled inside during the extension limit configuration (Fig. 5), were removed, as shown in Fig. 6, while the value of each dimension being kept identical to that in the original mechanism. As a result, the number of lateral sides reduced from 12 to 9. On using this modification, coiling motion does not occur during extension, and the mechanism can generate the tilting extension motion in all directions as well as pure vertical motion, as shown in Fig. 7. These motions could not be generated by the original 12-sided mechanism.

Third, an offset of the longitudinal sides was introduced, as shown in Figs. 6 and 7. In the original structure, collisions often occurred between each longitudinal side. In addition, the thickness of the components has a significant effect on these collisions, and the workspace narrows as the thickness increases. To decrease collisions while maintaining an adequate thickness of the components to ensure sufficient stiffness, an offset to the longitudinal sides was introduced in the outward direction, even though this would require idle revolute joints.

The novel mechanism was fabricated as a result of these improvements, as shown in Fig. 8. The dimensions are $a = 140$ mm, $b = 37.5$ mm, $m = 1$, $n = 12$, and $\varphi = \pi/12$. The revolute joints correspond to the mountain folded edges in the folding diagram and were physically realized using hinges of

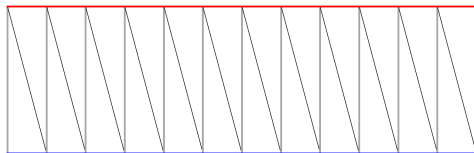
sufficient thickness and stiffness. This is unlike previous joints composed of thin materials such as paper, film, and cloth. To eliminate the revolute joint corresponding to the hypotenuse, components were added to connect that lateral sides using hinges. After these improvements, the mechanism was still considered to be equivalent to the kinematic model in a previous work [16]. To introduce the offset in the longitudinal sides, freely rotating idle revolute joints were added, thereby decreasing the collisions between each longitudinal side. As depicted in Fig. 8, one segment consists of two lateral chains and nine longitudinal sides. The lateral chain has hinges on both sides; therefore, additional segments can be connected by sharing these lateral chains.

C. DOF of one segment

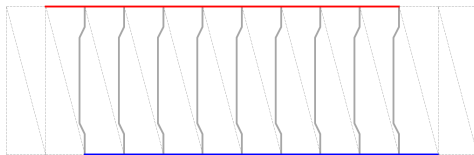
The DOF of the one segment novel mechanism was investigated using the loop closure equation. Regarding its structure without idle revolute joints, there are 43 revolute joints and nine kinematic chains, as indicated by the gray lines in Fig. 9, that connect the stationary link and the end effector. The nine equations for the velocity of the end effector are written as follows:

$$\left[\frac{\mathbf{s}_i}{\mathbf{P}_i \mathbf{P}_e \times \mathbf{s}_i} \right] \omega_i + \left[\frac{\mathbf{s}_{i+1}}{\mathbf{P}_{i+1} \mathbf{P}_e \times \mathbf{s}_{i+1}} \right] \omega_{i+1} + \dots = \mathbf{V}_{\mathbf{P}_e} \quad (1)$$

where \mathbf{P}_i is the position of each revolute joint, \mathbf{P}_e is the reference point of the end effector, \mathbf{s}_i is the unit vector along the axis of each revolute joint, ω_i is the angular velocity of



(a) The original 12-sided mechanism - unfolded



(b) The modified 9-sided mechanism with offset - unfolded

Fig. 6. One segment folding diagram of the 12- and 9-sided mechanisms

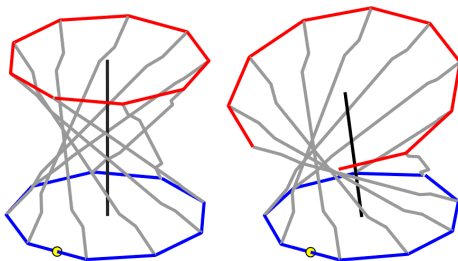


Fig. 7. Vertical and tilting extension motions achieved by decreasing the number of lateral sides from 12 to 9. The figure also reflects the offset of the longitudinal sides and the deformations of the longitudinal sides.

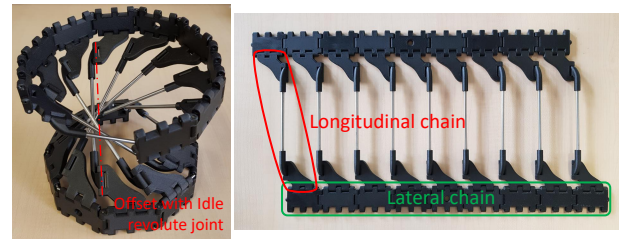


Fig. 8. Initial prototype of the novel mechanism. The kinematic chain, which consists of lateral side parts, is known as the lateral chain and is similar to the longitudinal chain. A majority of the parts are fabricated using 3D printers (Onyx One, Markforged), and stainless steel is used for the longitudinal parts to ensure high stiffness.

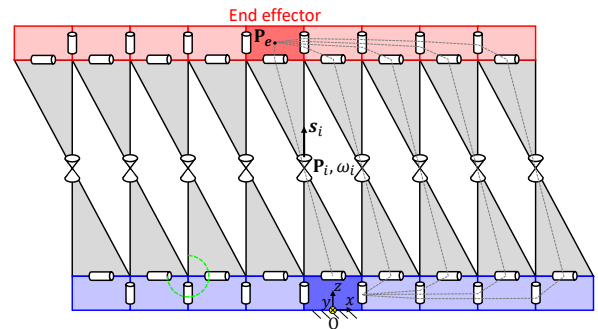


Fig. 9. Kinematic model for the loop closure equation. The stationary link is indicated in deep blue, and the end effector is indicated in deep red. There are nine kinematic chains, from the stationary link to the end effector. This kinematic model includes 43 revolute joints.

each revolute joint, and $\mathbf{V}_{P_e} = [\omega; v]$ is the velocity of the end effector. Based on these equations, eight loop closure equations with six dimensions can be derived by eliminating \mathbf{V}_{P_e} (i.e., 48 scalar equations). By combining them, the following equation is obtained:

$$\mathbf{A} \begin{bmatrix} \omega_1 \\ \omega_2 \\ \vdots \\ \omega_{43} \end{bmatrix} = 0 \quad (2)$$

where \mathbf{A} is the 48×43 coefficient matrix. By checking $\dim(\text{Ker}\mathbf{A})$, the number of independent angular velocities and the DOF can be derived. All configurations at the lattice point (angle step: 0.5 deg) $\dim(\text{Ker}\mathbf{A})$ were numerically investigated. The result showed that $\dim(\text{Ker}\mathbf{A})$ was always equal to three. Therefore, the DOF of the one segment novel mechanism is confirmed to be three, which is identical to that of the original design.

III. DISPLACEMENT ANALYSIS

A. One segment

To demonstrate the improvement of the workspace of the novel mechanism, a displacement analysis was performed. The definition of each point in the mechanism is shown in Fig. 10. L_j and U_j ($j = 1, 2, \dots, 10$) are the points in each lower and upper lateral chain, respectively, and C_L and C_U are the circumcenters of each lateral chain. In the displacement analysis, the inputs are θ_4 , θ_5 , and θ_6 (angle step: 0.5 deg), and the output is the position and orientation of coordinate $O' - x'y'z'$ at the middle of U_5 and U_6 , as shown in Figs. 10 and 11. The input space is defined as the region of θ_4 , θ_5 , and θ_6 at which the condition is satisfied; the condition is that

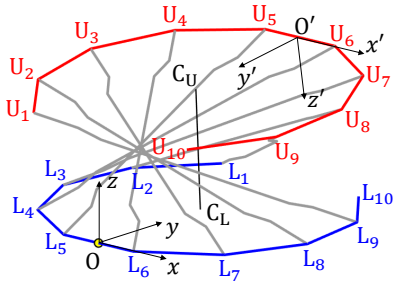


Fig. 10. Definition of points

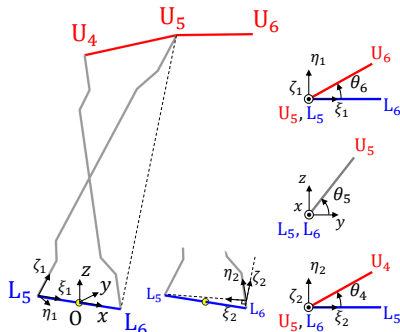


Fig. 11. Definition of inputs for one segment: θ_4 , θ_5 , and θ_6

the components do not interfere with each other. As a result, the input space of the novel mechanism is larger than that of the original mechanism for all cross sections of θ_5 , as shown in Fig. 12. This indicates that its workspace is much larger than that of the original, as shown in Fig. 13 and Table I, where the definitions of the tilt angle ψ and curvature radius ρ are depicted in Fig. 14. The right tilt angle is greater than the other angles by a factor of two, because there are fewer

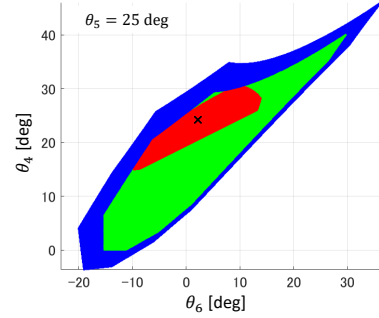


Fig. 12. Cross section of the input space at $\theta_5 = 25$ deg. The red area indicates the cross section of the original version with 12 lateral sides. The green area represents the cross section of the version with nine sides, without an offset. The blue area indicates the cross section of the novel mechanism. The input space becomes wider with the modification.

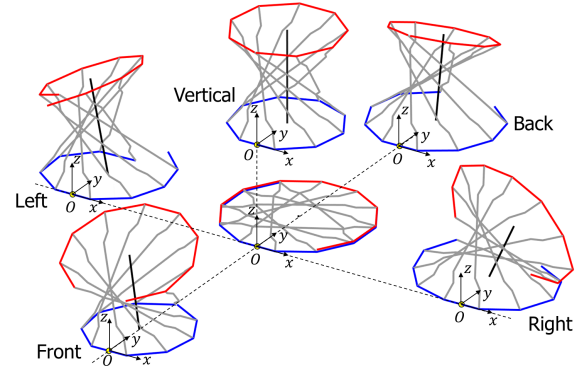


Fig. 13. Configurations at the boundary of the workspace. The figure shows the maximum tiling configuration along each direction and the maximum vertical extension.

TABLE I
METRICS OF THE CONFIGURATIONS AT THE WORKSPACE BOUNDARY

Direction	Max tilt angle ψ [deg]	Min curvature radius ρ [mm]
Front	21.6	114
Back	21.2	112
Left	24.6	210
Right	46.9	75.0
(Original)	(17.2)	(345)

*Initial radius: $a / \cos \phi = 72.5$ mm

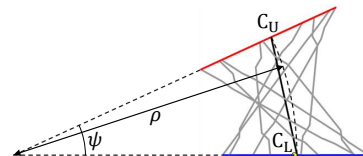


Fig. 14. Definition of tilt angle ψ and curvature radius ρ

longitudinal chains in the right as compared to those in the other directions, as you can see in Fig. 13. It is remarkable that the minimum curvature radius in the right direction can be as small as the initial radius of this mechanism. In addition, the minimum curvature radius and the largest tilt angle can be simultaneously generated. Thus, the novel mechanism can generate a configuration with a large curvature, using a few segments. This is a distinct advantage of this mechanism.

Now, the three inputs of a segment can be redefined as $\|\overrightarrow{L_1L_{10}}\|$, $\|\overrightarrow{U_1U_{10}}\|$, and θ_i ; the angle of $\overrightarrow{L_1L_{10}}$ against x axis is shown in Fig. 15. Among these three inputs, the difference in the two distances $\|\overrightarrow{L_1L_{10}}\|$ and $\|\overrightarrow{U_1U_{10}}\|$ generates the tilting motion in the front/back, and the positive/negative angle θ_i generates the tilting motion in the left/right.

B. Multiple segments

To perform the displacement analysis corresponding to the motion of the prototype, the DOF of the novel mechanism with multiple segments is considered.

To reveal the extent of change in the configurations of the novel and original mechanisms where the lower point's positions are almost fixed, the possible configurations were explored. As the indices for comparison, the ranges of the normal vector of the upper plane and the length $\|\overrightarrow{U_1U_{10}}\|$ were analyzed for the condition where 10% of the representative length a is the maximum change in the position of the lower point. The middle point of the input space of the original 12-sided version shown in Fig. 12 is considered as an example. In Fig. 16, the black line represents the normal vector of this configuration, and the three areas depict the range of the normal vector of the upper plane. As shown in Fig. 16, the normal vector range of the novel mechanism is wider than that of the original mechanism, especially along the direction of the y axis. The range of $\|\overrightarrow{U_1U_{10}}\|$ is presented in Table II. The range of $\|\overrightarrow{U_1U_{10}}\|$ of the novel mechanism is 88 mm; this is 86% of the maximum range and exceeds the range of the original mechanism by a factor of 2.4.

These results reveal that the novel mechanism has additional possible configurations and the potential to dramatically change its configuration with small errors at the lower positions of each segment. Therefore, when the configuration of a segment is decided using three inputs (i.e., $\|\overrightarrow{L_1L_{10}}\|$, $\|\overrightarrow{U_1U_{10}}\|$,

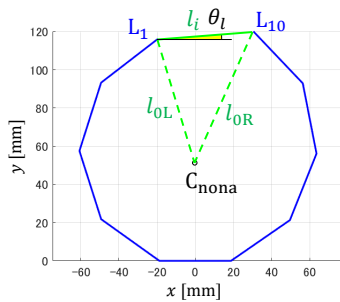


Fig. 15. Two inputs in the lower lateral chain: $\|\overrightarrow{L_1L_{10}}\|$ and θ_i , and the relation between l_i , θ_i , l_{0L} , and l_{0R} . C_{nona} is the center of the nonagon when the mechanism is fully extended.

and θ_i), its two adjacent segments need another input to decide each of their configurations in a mechanism with multiple segments. Each lateral chain is shared by the two adjacent segments, except the base and top segments, as shown in Fig. 17. With respect to a lateral chain, the two inputs of the upper segment, $\|\overrightarrow{L_1L_{10}}\|$ and θ_i , are already determined by the lower segment. Therefore, the bottom segment requires three inputs, and the other segments require a single input $\|\overrightarrow{U_1U_{10}}\|$ to determine their configurations. To summarize, a mechanism with m segments has $m + 2$ DOF, and a practical example of the input variables are the lengths l_i ($i = 0, 1, \dots, m$) and θ_i in the base lateral chain.

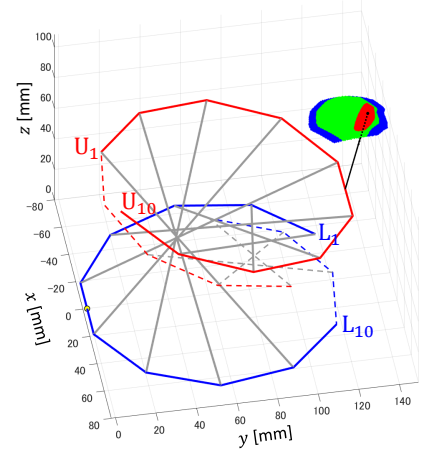


Fig. 16. Comparison of possible configurations. This configuration corresponds to the inputs of the point in Fig. 12. The black line represents the normal vector of the upper plane. The three areas around the end of the black line represent the movement of the normal vector within the permissible change in the shape of the lower lateral side. Similar to Fig. 12, each color represents a different version of the mechanism.

TABLE II
RANGE OF THE LENGTH $\|\overrightarrow{U_1U_{10}}\|$

Type of mechanism	Range of distance [mm]
12 sides ver.	36
9 sides ver.	83
9 sides offset ver.	88

*Maximum range: 102mm

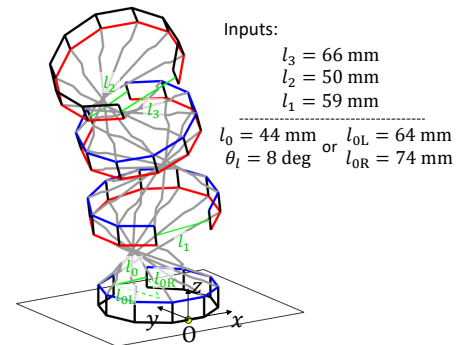


Fig. 17. Example of the entire configuration of the mechanism with multiple segments obtained via displacement analysis. The lookup table method is applied with five input values for mechanism with three segments.

Displacement analysis of the multiple segments can be performed using the input variables; however, it is complicated to directly derive a configuration based on the lengths l_i and angle θ_l . Therefore, for simplicity, the lookup table method was employed. The table for one segment was created as follows:

- 1) Provide the three input angles for the displacement analysis of one segment: θ_4 , θ_5 , and θ_6 ;
- 2) Gather configurations that satisfy the conditions;
- 3) Calculate l_i , l_{i+1} and θ_l for each configuration;
- 4) Create a table with the relationships between $(\theta_4, \theta_5, \theta_6)$ and (l_i, l_{i+1}, θ_l) .

Based on the input variables: lengths l_i and the angle θ_l , the configuration of each segment can be selected from the table, from the bottom segment to the top segment. As an example, a configuration of the three-segment mechanism is presented in Fig. 17 with five inputs variables: l_0 , l_1 , l_2 , l_3 , and θ_l .

IV. PROOF OF CONCEPT

A. Actuation method

To develop an actuated prototype based on the example of the input variables in section III B, we considered a number of design principles: the actuators must be placed at the center of the lateral chain and symmetry should be maintained, the input values should be observable, and the actuators on the upper segments should be sufficiently small to fit in the inner space. Moreover, the torque output of the actuator is related to, and limited by, the size of the actuator. Consequently, the wire driven strategy by a rotary actuator is introduced, because the output torque of the rotary actuator can be adjusted by changing the pulley diameter. Similar to the general wire driven strategy, a leaf spring is inserted to apply tension on the wire for the counter actuation.

The prototype with three segments consists of four lateral chains, as shown in Fig. 18, and requires five inputs based on the discussion of DOF in section III B: l_0 , l_1 , l_2 , l_3 , and θ_l . About two inputs in the base lateral chain: l_0 and θ_l , it is much more effective and simpler to change two wire lengths than one wire length and its angle. Therefore, l_0 and θ_l are replaced by l_{0L} and l_{0R} , as shown in Fig. 15. C_{nona} is the center of the nonagon when the mechanism is fully extended. According to this replacement, the information regarding l_{0L} and l_{0R} is added to the table for the displacement analysis of multiple segments, as shown in Fig. 17. The blue lateral chain represents the base lateral chain, which includes the stationary part, and the red lateral chain represents the upper lateral chains. The base lateral chain (Fig. 19) includes two actuators (FAULHABER, Brushless DC motor, 3042W036C) to pull two wires and change l_{0L} and l_{0R} . To ensure that the lengths of the input wire are observable regardless of the configuration, the wires pass through the corners of the polygon. The leaf spring is only fixed to the stationary part to ensure that it can slide against the other lateral side parts, when the shape of the lateral chain changes. In addition, the upper lateral chain (Fig. 20) has one actuator (Copal Electronics, Stepping motor, SPG20-1332, max torque: 75 mN·m) that fits in the inner space. The wire path and leaf spring are identical to those

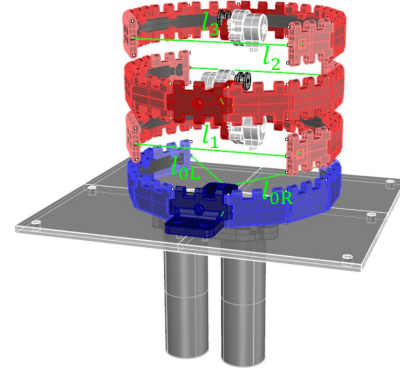


Fig. 18. Complete design of the extendable arm. The five inputs are l_{0L} , l_{0R} , l_1 , l_2 , and l_3 .

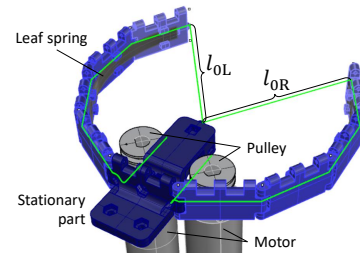


Fig. 19. Design of the base lateral chain. The distance and angle between the two edges are determined based on the length of the two wires. To measure the input length, regardless of the configuration, the wires pass through the corners of the polygon, where the path length is constant.

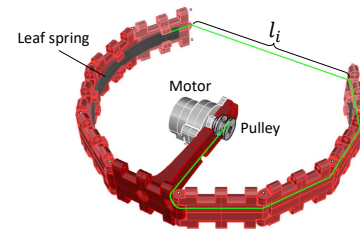


Fig. 20. Design of the upper lateral chain. Similar to the base lateral chain, the wires pass through the corners of the polygon.

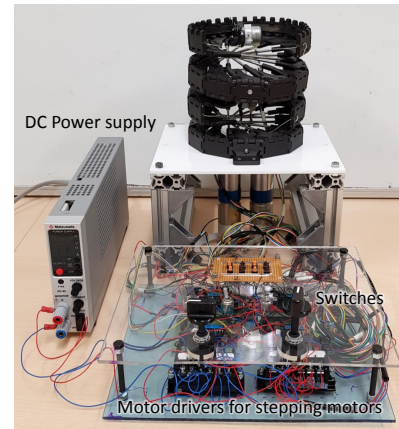


Fig. 21. Experimental setup. The prototype is manually controlled using five analog switches.

in the base lateral chain. The maximum velocity ratio of input to output is 1:2.2, where the input velocity is relative velocity between L_1 and L_{10} (or U_1 and U_{10}), and the output velocity is the velocity of the end effector. This ratio is relatively larger than that of a general parallel mechanism, which shows that the extendable mechanism designed in this paper is characterized as a high speed and low payload capacity mechanism. In order to support the payload on the end effector by the small actuator shown above, the radius of the small pulley was decided to be 3.2 mm for actuating the upper two segments (one segment: 169 g).

The loop closure equation as same in section II C is used to confirm that this actuation method gives proper inputs to the mechanism, with following equation;

$$\mathbf{A}_a \boldsymbol{\omega}_a + \mathbf{A}_p \boldsymbol{\omega}_p = 0 \quad (3)$$

where $\boldsymbol{\omega}_a$ is the 3×1 vector with angular velocities of three chosen active revolute joints, $\boldsymbol{\omega}_p$ is the 40×1 vector with angular velocities of 40 passive revolute joints, \mathbf{A}_a is the 48×3 coefficient matrix, and \mathbf{A}_p is the 48×40 coefficient matrix. The matrix \mathbf{A} in (2) is divided into \mathbf{A}_a and \mathbf{A}_p according to distinction of joints between active and passive. When the three chosen revolute joints are independent, $\dim(\text{Ker}\mathbf{A}_p)$ is

0; these joints are appropriate as active joints. All combinations of three joints among 43 joints have been investigated. When three joints are chosen from a same spherical chain as shown by green line in Fig. 9, $\dim(\text{Ker}\mathbf{A}_p)$ becomes 1, which means that one active joint is dependent on the others. However, for every combinations except the combinations above, $\dim(\text{Ker}\mathbf{A}_p)$ is equal to 0. The introduced actuation method, which changes the distance between two ends of each lateral chain, is not the exception and gives appropriate inputs to the mechanism.

B. Motion Experiment

The setup for the prototype motion experiment is presented in Fig. 21. We applied 13 V and 2.00 A to each DC motor and 13 V and 0.30 A to each stepping motor. The prototype was manually controlled using five analog switches. The extension ratio was 290%, increasing from 135 mm to 392 mm. Actually, the extension ratio was significantly influenced by the width of the lateral side part. If the width were to be decreased to zero, the extension ratio could a maximum value of 592%, increasing from 48 mm to 284 mm.

To validate the availability of the actuation method, extensional and contractional motions (Fig. 22, duration: 96

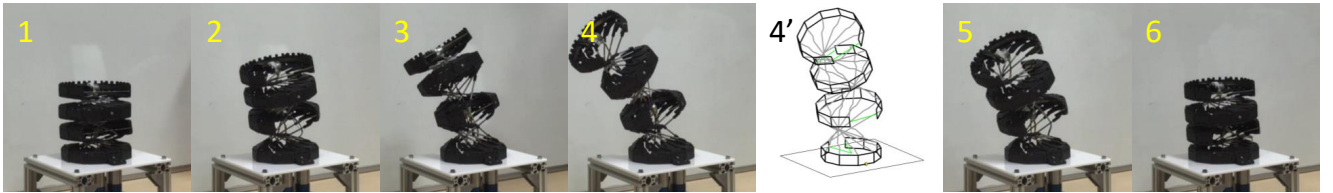


Fig. 22. Extension and contraction. The output configuration at the 4th frame is compared with the result of the displacement analysis. This configuration is based on the following inputs: $l_{0L} = 64$, $l_{0R} = 74$, $l_1 = 59$, $l_2 = 50$, and $l_3 = 66$ mm. The prototype approximately achieves the desired configuration, although a few errors exist.

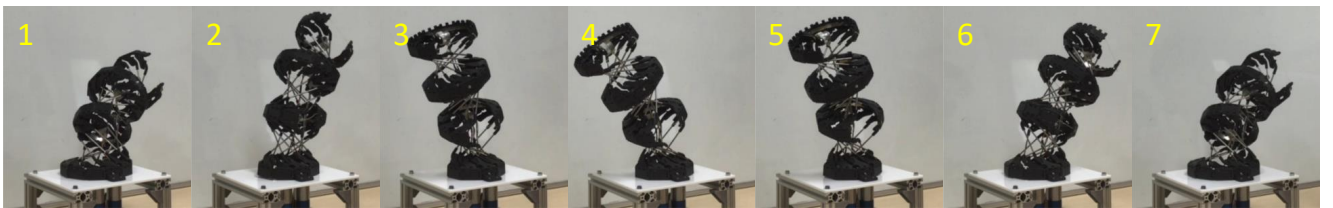


Fig. 23. Swinging from right to left and vice versa. When l_{0L} is longer than l_{0R} , the prototype tilts to the right. Conversely, when l_{0R} is longer than l_{0L} , the prototype tilts to the left.

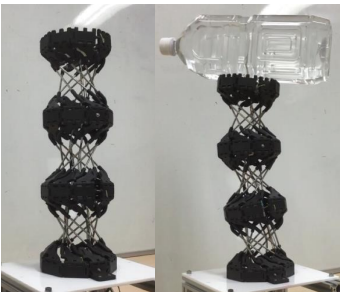


Fig. 24. Fully extended shape and load trial, using a 2-L plastic bottle filled with water as the vertical load

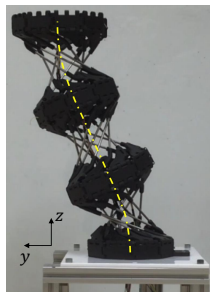
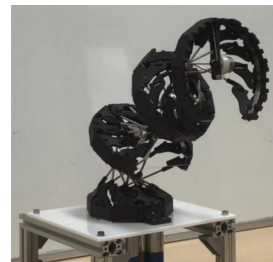
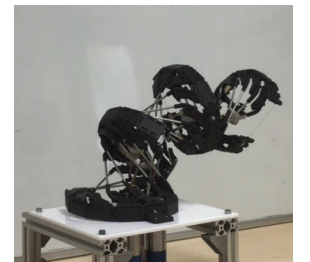


Fig. 25. Example of an S-shape configuration with inflection points



(a) Front



(b) Right

Fig. 26. Generation of maximum tilting configurations at the workspace boundary corresponding to Fig. 13. (b) In this configuration, the curvature attains its maximum value.

sec.), swing motions from right to left and vice versa (Fig. 23, duration: 56 sec.), and full extensional (392 mm height) and load trials (Fig. 24) were conducted. First, the prototype could successfully go back to the fully contracted configuration through the extension and contraction. Second, the prototype approximately achieved the desired configuration (inputs: $l_{0L} = 64$, $l_{0R} = 74$, $l_1 = 59$, $l_2 = 50$, $l_3 = 66$ [mm]) when compared with the displacement analysis, although a few errors were observed. These errors were mainly attributed to the compliance of the mechanism. Third, the expected swing motion was achieved, owing to the difference in the input length between l_{0L} and l_{0R} . Fourth, when the prototype is fully extended, it has a moderate stiffness exceeding 19.6 N against the vertical load. In addition, various configurations were generated, including S-shapes (Fig. 25), and maximum tilting configurations to the front (Fig. 26a) and to the right (Fig. 26b) were also achieved. The achievable, minimum curvature radius for the S-shape configuration is 114 mm. The tilt angle ψ and curvature radius ρ of each segment in the maximum tilting configurations are corresponding to the values in Table I.

These motion experiments confirmed the validity of the design and the actuation method presented in this paper. About the method of actuating the base lateral chain, it is appropriate to ensure a difference between l_{0L} and l_{0R} , which is equal to the angle θ_l , as shown in Fig. 23. Furthermore, it is also appropriate to shorten the length l_0 , except the end of the extension in which the base lateral chain needs to be completely closed such that $l_0 = 0$. This insufficiency leads to the errors mentioned above. To address this issue, an additional wire having the same path as the upper lateral chain can be introduced as a possible solution.

V. CONCLUSIONS

In this paper, we introduced the design of a novel rigid extendable arm, which has multiple DOF, while improving the configuration transformability of the original origami structure by removing the part at which undesired deformations occur.

The design process of the novel extendable mechanism is demonstrated, and the prototype is fabricated using rigid components. The novel extendable mechanism has been proven to be a sophisticated and suitable mechanism that can be implemented in extendable arms. The number of inputs is clarified by considering the range of possible configurations with small errors, and the actuation method is determined based on the result of the confirmation, using the loop closure equation. The proposed novel extendable arm can generate various configurations, including a configuration with a large curvature. Furthermore, the validity of the proposed design has also been confirmed.

In future work, to improve the stability of the configuration and the smoothness in the motion of the extendable arm, the transmissibility of force and motion will be considered with regard to the following points: static force and elastic deformation, the effects of clearance and friction in joints, and the evaluation of system properties for diverse configurations.

REFERENCES

- [1] K. Miura, "The science of miura-ori: A review," *Origami*, vol. 4, pp. 87–100, 2009.
- [2] T. Tachi, "Rigid-foldable thick origami," *Origami*, vol. 5, pp. 253–264, 2011.
- [3] B. J. Edmondson, R. J. Lang, S. P. Magleby, and L. L. Howell, "An offset panel technique for thick rigidly foldable origami," in *ASME 2014 International Design Engineering Technical Conferences and Computers and Information in Engineering Conference*. American Society of Mechanical Engineers, 2014, pp. V05BT08A054–V05BT08A054.
- [4] Y. Chen, R. Peng, and Z. You, "Origami of thick panels," *Science*, vol. 349, no. 6246, pp. 396–400, 2015.
- [5] E. T. Filipov, T. Tachi, and G. H. Paulino, "Origami tubes assembled into stiff, yet reconfigurable structures and metamaterials," *Proceedings of the National Academy of Sciences*, vol. 112, no. 40, pp. 12321–12326, 2015.
- [6] M. R. Morgan, R. J. Lang, S. P. Magleby, and L. L. Howell, "Towards developing product applications of thick origami using the offset panel technique," *Mechanical Sciences*, vol. 7, no. 1, pp. 69–77, 2016.
- [7] R. V. Martinez, C. R. Fish, X. Chen, and G. M. Whitesides, "Elastomeric origami: programmable paper-elastomer composites as pneumatic actuators," *Advanced functional materials*, vol. 22, no. 7, pp. 1376–1384, 2012.
- [8] J. Santoso, E. H. Skorina, M. Luo, R. Yan, and C. D. Onal, "Design and analysis of an origami continuum manipulation module with torsional strength," in *2017 IEEE/RSJ International Conference on Intelligent Robots and Systems (IROS)*. IEEE, 2017, pp. 2098–2104.
- [9] D. Jeong and K. Lee, "Design and analysis of an origami-based three-finger manipulator," *Robotica*, vol. 36, no. 2, pp. 261–274, 2018.
- [10] J. Fathi, O. V. T. JC, M. S. Runciman, and G. P. Mylonas, "A deployable soft robotic arm with stiffness modulation for assistive living applications," in *2019 International Conference on Robotics and Automation (ICRA)*. IEEE, 2019, pp. 1479–1485.
- [11] J. Cai, X. Deng, Y. Zhang, J. Feng, and Y. Zhou, "Folding behavior of a foldable prismatic mast with kresling origami pattern," *Journal of Mechanisms and Robotics*, vol. 8, no. 3, p. 031004, 2016.
- [12] Z. Wu, I. Hagiwara, and X. Tao, "Optimisation of crush characteristics of the cylindrical origami structure," *International Journal of Vehicle Design*, vol. 43, no. 1–4, pp. 66–81, 2007.
- [13] S. Ishida, K. Suzuki, and H. Shimosaka, "Design and experimental analysis of origami-inspired vibration isolator with quasi-zero-stiffness characteristic," *Journal of Vibration and Acoustics*, vol. 139, no. 5, p. 051004, 2017.
- [14] J. Beynon, "Spring into action, bos magazine, vol. 142," *British Origami Society*, 1990.
- [15] H. Matsuo, D. Matsuura, Y. Sugahara, and Y. Takeda, "Kinematic characterization of the origami spring based on a spherical 6r linkage," in *New Advances in Mechanisms, Mechanical Transmissions and Robotics*. Springer, 2017, pp. 187–196.
- [16] —, "Modeling and displacement analysis of origami spring considering collision and deformation of components," in *IFTOMM World Congress on Mechanism and Machine Science*. Springer, 2019, pp. 329–336.